Volume 15
Number 22
21 November 2025
Pages 6571–6914

Catalysis Science & Technology

rsc.li/catalysis

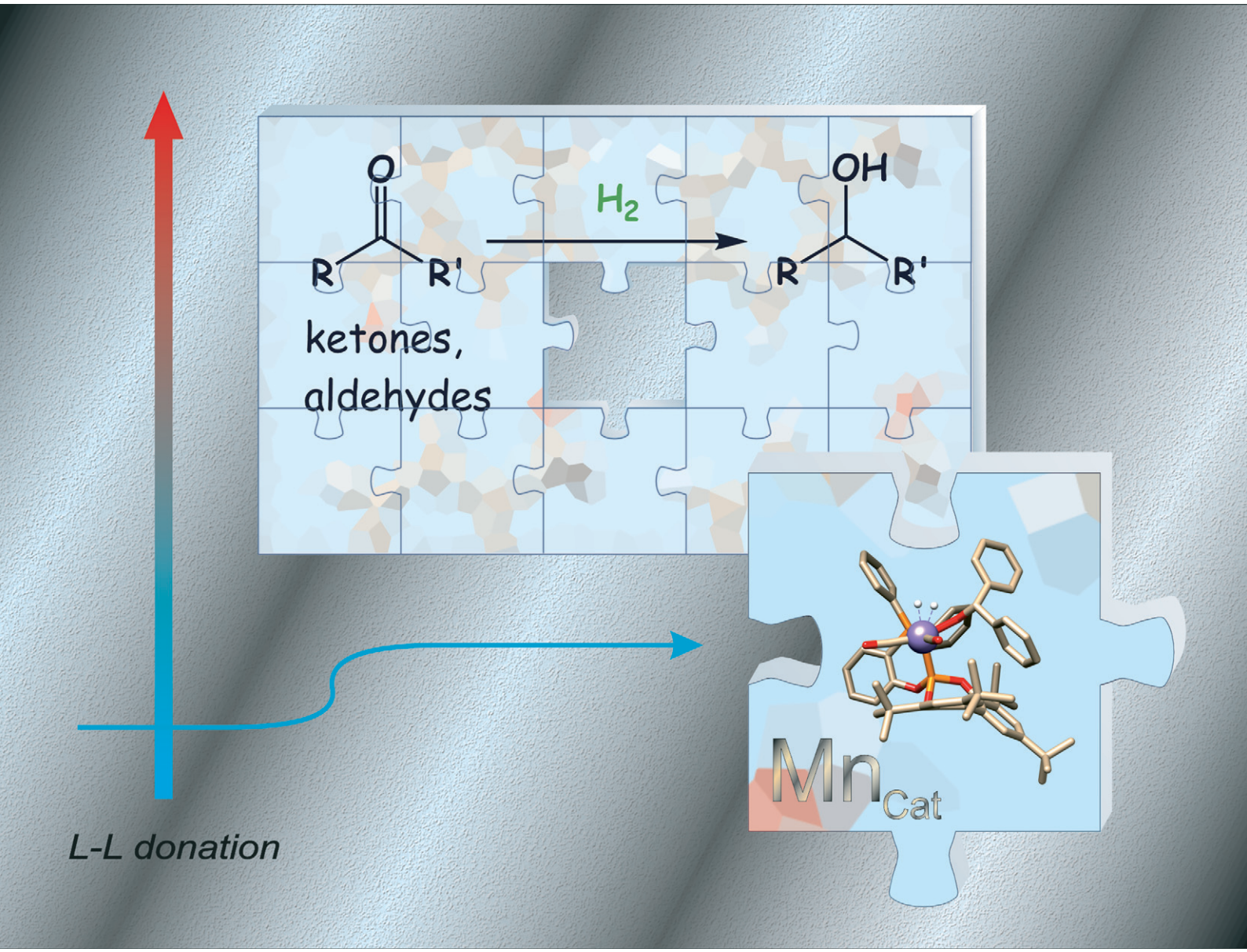

ISSN 2044-4761

ROYAL SOCIETY OF CHEMISTRY

PAPER

Joaquín López Serrano, Antonio Pizzano *et al.*
Non-bifunctional Mn catalysts based on phosphine–phosphites for the hydrogenation of carbonyl substrates

Catalysis Science & Technology

ROYAL SOCIETY OF CHEMISTRY

PAPER

View Article Online
View Journal | View Issue

Check for updates

Cite this: *Catal. Sci. Technol.*, 2025, 15, 6666

Non-bifunctional Mn catalysts based on phosphine–phosphites for the hydrogenation of carbonyl substrates

Verónica Jiménez,† Carmen González,† Joaquín López Serrano, * Francisco Fernández de Córdova and Antonio Pizzano *

Received 24th July 2025,
Accepted 19th September 2025

DOI: 10.1039/d5cy00906e

rsc.li/catalysis

A series of Mn(I) complexes bearing phosphine–phosphite ligands (P-OP) of formula [Mn(Br)(P-OP)(CO)$_3$] (**1**) have been prepared and characterised. These compounds exist in solution as a mixture of *fac* and *mer* isomers with *fac/mer* ratios from 18 : 1 to 2 : 1. The relatively low donor ability of P-OP compared to bis(trialkylphosphines) or bis–NHC ligands, typically found in non-bifunctional Mn catalysts reported to date, is evinced in IR spectra. Compounds **1** provide efficient catalysts for the hydrogenation of carbonyl substrates using KO*t*Bu as a base. Notably, these complexes constitute a set of modularly designed precatalysts and optimisation of the P-OP ligand provided appropriate catalysts for the reduction of a wide variety of aldehydes and ketones under mild reaction conditions (S/C = 250–500, 20 bar H_2, RT to 40 °C). A mechanistic study combining spectroscopic and computational results provides support for a catalyst activation process based on the nucleophilic attack of the alkoxide on a coordinated CO in [Mn(O*t*Bu)(P-OP)(CO)$_3$], as well as a non-bifunctional inner-sphere hydrogenation pathway in the representative hydrogenation of benzophenone. The catalytic cycle is also characterised by a rather stable pentacoordinated alkoxide [Mn(k^1-*O*–OCHPh$_2$)(P-OP)(CO)$_2$] which determines the energetic span of the reaction.

Introduction

The search for cost-effective alternatives to well-established noble metal catalysts is one of the more important research topics in homogeneous hydrogenation.[1] In this regard, Mn catalysts have already shown particularly promising results in terms of broad substrate scope and catalyst activity.[2] This field emerged a decade ago with prominent examples of bifunctional catalysts,[3] which boosted the research on this type of systems.[4,5] Alternatively, non-bifunctional ones have remained much less explored and are notably restricted to derivatives of highly donating bidentate ligands. The corresponding catalyst precursors have the formula Mn(X)(L–L)(CO)$_3$ where X denotes an anionic ligand such as Br, alkyl or triflate, while L–L corresponds to bis(trialkylphosphine) or to NHC based ligands. For instance, complex **A** (X = Br, R = *n*Pr; Fig. 1)[6a] provides an active catalyst for the hydrogenation of ketones and nitriles, while for the latter a triflate derivative (R = *i*Pr) reported by the group of García operated under milder conditions.[7] Moreover, Kirchner and coworkers have demonstrated that alkyl compound **B** has a remarkable reactivity in hydrogenation and is capable to reduce without the need of base ketones, alkenes, alkynes and CO_2.[6b–e] On the other hand, bis–NHC derivatives **C** (ref. 8) provide outstanding results in the challenging hydrogenation of esters.[9,10] An example of this type developed by Beller and coworkers (R = R′ = Me) exhibits a broad scope and also hydrogenates a wide variety of ketones, nitriles and olefins.[10] Finally, the group of Sortais has reported an interesting case of a complex based on a NHC–thioether ligand (**D**) which leads to an active catalyst for the hydrogenation of olefins and ketones.[11] These precedents raise the question of whether it is possible to expand catalyst activity in hydrogenation reactions to less donating ligands (*e.g.* arylphosphines, phosphoramidites, phosphites).[12] This is an

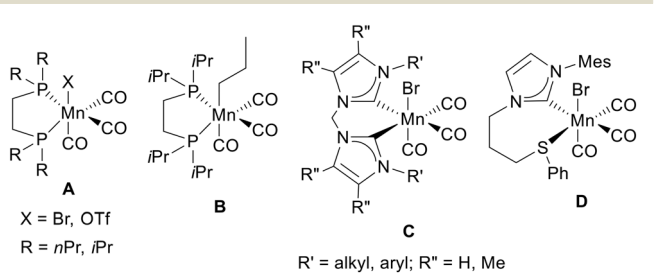

Fig. 1 Structure of compounds **A**–**D**.

Instituto de Investigaciones Químicas and Centro de Innovación en Química Avanzada (ORFEO-CINQA), CSIC and Universidad de Sevilla, Avda Américo Vespucio 49, 41092 Sevilla, Spain. E-mail: joaquin.lopez@iiq.csic.es, pizzano@iiq.csic.es

† These authors have contributed equally to this work.

area with a high potential due to the vast structural diversity of these P-ligands, which span a wide range of electronic and steric properties, features that are most useful for comprehensive catalyst optimisation.[13]

In our laboratory we have been interested in the study of phosphine–phosphite ligands (P-OP) in Rh, Ir and Ru catalytic hydrogenation,[14] while applications in other catalytic processes such as hydroformylation (Rh),[15] conjugate addition or alkylation (Cu)[16] cycloaddition (Au)[17] or hydrocyanation reactions (Ni),[18] have also been described. These ligands are characterized by an easily tuneable structure and a π-acceptor phosphite fragment which makes them less donor than ubiquitous diphosphines,[19] while the different electronic properties of their P fragments cause important directing effects in catalysis.[20] In this contribution we report the first application of P-OP ligands in Mn catalysed hydrogenation. Complexes prepared show good activity in the hydrogenation of a wide variety of ketones and aldehydes under mild reaction conditions, while complementary spectroscopic and computational results provide support for a low-barrier catalyst activation pathway and a non-bifunctional inner-sphere hydrogenation mechanism.

Results and discussion

Synthesis and characterization of Mn phosphine–phosphite complexes

Compounds [Mn(Br)(P-OP)(CO)$_3$] (**1a–1d**) were obtained in high yields from [Mn(Br)(CO)$_5$] and a stoichiometric amount of P-OP ligand (**L1–L4**, respectively; Scheme 1). Moreover, **1a** reacts with AgOTf to give [Mn(OTf)(**L1**)(CO)$_3$] (**2a**), while the latter reacts with KBH_4 to give the corresponding hydride [Mn(H)(**L1**)(CO)$_3$] (**3a**). For these complexes, four isomers can be distinguished: two chiral facial isomers, *fac1* and *fac2* (Fig. 2), which differ in metal configuration, and two meridional isomers *mer1* and *mer2*, which can be differentiated by the relative positions of the X and P atoms. The *fac* isomers can be notated as *OC-6-44-C* and *OC-6-44-A*, respectively,[21] although for simplicity, *C* (*fac1*) and *A* (*fac2*) will be used to refer to metal configuration. It is important to note that a stereogenic axis in the biaryl is generated upon phosphite coordination. However, a fast atropisomerization of the biaryl fragment at room temperature is expected, as observed before in Rh (ref. 22) and Ru (ref. 20*b*) complexes containing these P-OP ligands.

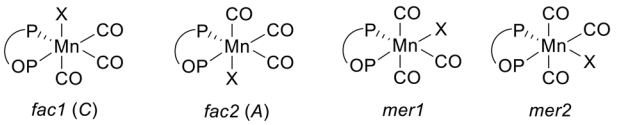

Fig. 2 Structure of isomers of complexes **1–3**.

Characterisation in solution of compounds **1** show a mixture of two isomers, with the *fac* isomer being predominant, and *fac*/*mer* ratios from 18 : 1 (**1c**) to 2 : 1 (**1d**). This is an interesting difference with diphosphine derivatives [Mn(Br)(P–P)(CO)$_3$] which solely exist in solution as *fac* isomers.[6a,23] For compounds **1** comparison of $^{31}P\{^1H\}$ NMR spectra show distinct data for the two isomers, thus J_{PP} coupling constants are between 12 and 17 Hz higher in the *fac* isomer. In addition, there is a marked low field shift ($\Delta\delta$ = 27–30 ppm) of the phosphite signal of the *mer* isomer compared to the *fac* one (Fig. 3a). Due to the relatively high concentration of *mer*-**1d**, full characterization in solution from ^1H and $^{13}C\{^1H\}$ NMR (Fig. 3b) has been possible for this isomer. In contrast, for the triflate derivative **2a**, the isomer ratio is 24 : 1, while for hydride **3a** only the *fac* isomer was

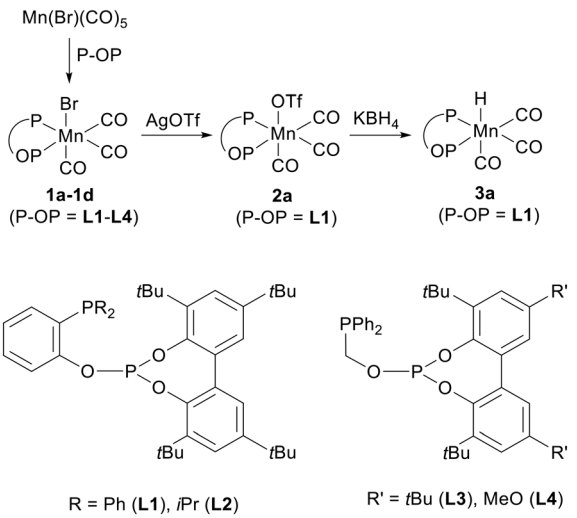

Scheme 1 Synthesis of complexes **1–3**.

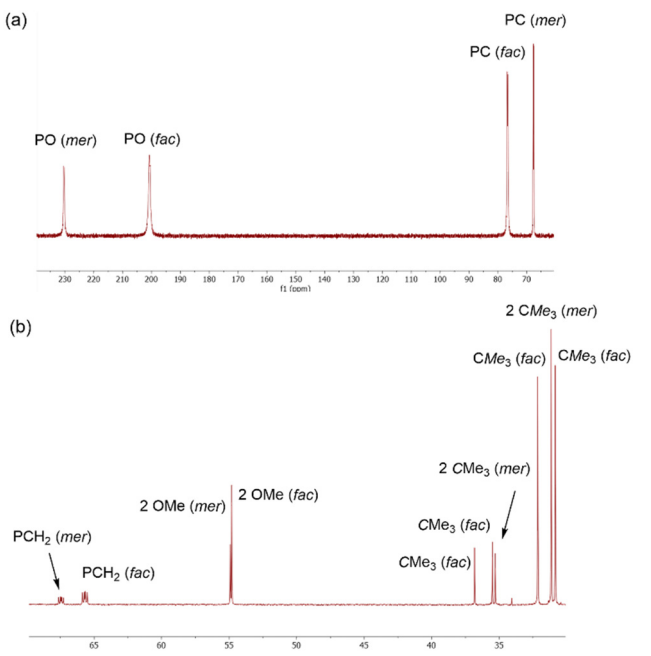

Fig. 3 (a) $^{31}P\{^1H\}$ NMR (C_6D_6, 202 MHz) spectrum of **1d** and (b) aliphatic region of $^{13}C\{^1H\}$ NMR (C_6D_6, 125 MHz) spectrum of **1d**.

observed. Moreover, the observation of three strong bands in the carbonyl region of IR spectra of complexes **1–3** is also consistent with the *fac* isomer (*e.g.* 2030, 1969 and 1943 cm^{-1} for **1a**). Nevertheless, less intense bands attributable to minor *mer* isomers have also been detected (*e.g.* 1987 and 1960 cm^{-1} for **1a**). With the available spectroscopic data, it is not possible to ascertain the stereochemistry of the *mer* isomer, although it is reasonable to propose a *mer1* structure in which CO and phosphite avoid mutually *trans* positions. These assumptions will be further supported by DFT calculations (see below). Compound **1a** has been studied by ^{1}H and $^{31}P\{^{1}H\}$ NMR at low temperature with the aim of freezing phosphite atropisomerization. However, down to −80 °C, no significant lineshape changes in these spectra were observed, indicating that atropisomerization is still fast at this temperature. This compound has also been characterized by single crystal X-ray crystallography (Fig. 4). In the crystal lattice a racemic mixture composed by *C*,S_{ax} and *A*,R_{ax} isomers was observed. Thus, stereoisomers differing in the relative metal and biaryl configuration (*i.e. C*, R_{ax} and *A*,S_{ax}) should be less stable.

An interesting difference between compounds **1** and non-bifunctional catalyst precursors found in literature concerns the lower electron density at the metal centre in the former. This is evidenced by the position of υ(CO) bands in IR spectra. Thus, the bands of **1a** appear at higher frequencies than those of **A** (X = Br, R = *n*Pr; 2003, 1935 and 1903 cm^{-1}),[6a] **C** (R′ = R″ = Me; 1995, 1908 and 1868 cm^{-1})[10] and **D** (2010, 1925 and 1894 cm^{-1}).[11] A similar trend is observed when by comparing **2a** or **3a** with their 1,2-bis(diphenylphosphino) ethane analogues.[24]

To complete the study, we have investigated the relative stability of the isomers of representative complexes **1a** (Fig. 5) and **1c** by DFT methods.[25] For the sake of clarity, the S_{ax} configuration at the biaryl was selected throughout the study. In the case of **1a**, the most stable structure corresponds to *fac1*-**1a**, matching the structure observed by X-ray crystallography, while diastereomeric *fac2*-**1a** is 2.8 kcal mol^{-1} higher in free energy. In addition, *mer1*-**1a** is 3.7 kcal mol^{-1} less stable than *fac1*-**1a**, while *mer2*-**1a** is the least stable isomer (6.4 kcal mol^{-1}). For **1c**, the preferred structure is *fac2*-**1c**, while the *fac1*, *mer1* and *mer2*

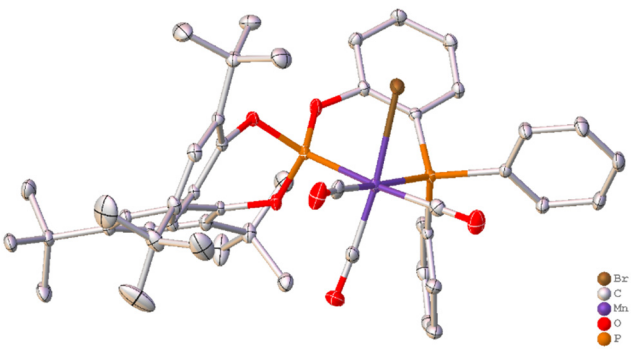

Fig. 4 ORTEP view of *C*,S_{ax} isomer of complex **1a** (H atoms have been omitted for clarity).

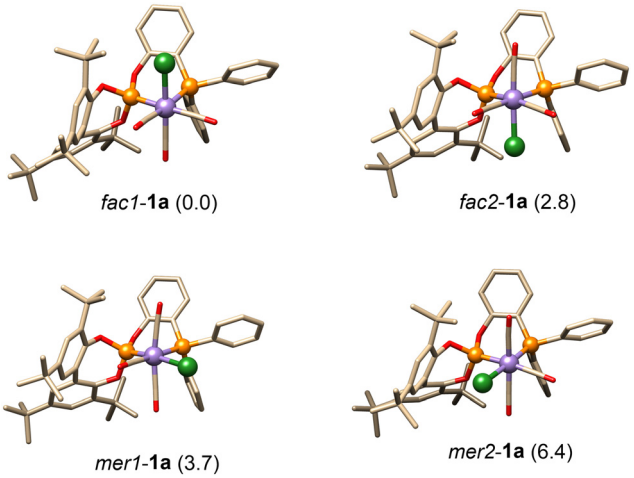

Fig. 5 Optimized geometries of isomers of **1a**. Numerical values correspond to free energies relative to *fac1* isomer (kcal mol^{-1}, hydrogens have been omitted for clarity).

isomers lie 3.2, 2.9 and 7.0 kcal mol^{-1} higher in free energy, respectively. Likewise, analysis of the isomers of **3a** showed that the *fac1* isomer is the more stable, with the *fac2*, *mer1* and *mer2* structures lying 2.1, 3.8 and 5.2 kcal mol^{-1} above *fac1*-**3a**, respectively. These results are consistent with the experimental preference for the *fac* isomer, while the small energy differences observed between *fac1* and *fac2*, besides a fast atropisomerization, suggest a mixture of these facial isomers in solution, along with minor amounts of *mer1*. In contrast, *mer2* isomers can be disregarded due to their significantly higher energies. Similarly, a difference of 7.9 kcal mol^{-1} between **A** (X = Br, R = *n*Pr) and the corresponding *mer* isomer has been reported.[6a]

Catalytic hydrogenation of carbonyl compounds

To examine the potential of compounds **1** in catalytic hydrogenation, we first carried out a series of hydrogenations of acetophenone with these complexes under relatively mild reaction conditions in *i*PrOH using KO*t*Bu as a base (20 bar H_2, RT, S/C/B = 500/1/10). We were pleased to observe that complex **1a** provided nearly full conversion under these conditions (entry 1; Table 1), while the remaining complexes gave moderate values (65, 53 and 61 %, for **1b–1d**, entries 2–4 respectively). From these results, we selected **1a** for further optimisation. First, the use of alternative solvents was examined, with satisfactory results obtained in toluene (entries 5, 7), while lower activity was observed in CH_2Cl_2 (entry 6). We then attempted to lower the catalyst loading. In this regard, it was observed that increasing the base concentration led to a decrease in conversion (entries 9–12). Notably, increasing the reaction temperature proved detrimental in both toluene (entries 13, 14) and *i*PrOH (entry 15). Finally, a mercury drop test indicated that the reaction is homogeneous (entry 16). In contrast to **1a**, the triflate complex **2a** showed reduced activity (entries 17, 18), while a reaction with hydride **3a** in the absence of base lead to

Table 1 Hydrogenation of acetophenone with catalyst precursors **1–3**[a]

Entry	Complex	Solvent	S/C/B	Temp. (°C)	Conv. (%)
1	**1a**	*i*PrOH	500/1/10	RT	99
2	**1b**	*i*PrOH	500/1/10	RT	65
3	**1c**	*i*PrOH	500/1/10	RT	53
4	**1d**	*i*PrOH	500/1/10	RT	61
5	**1a**	Toluene	100/1/10	RT	100
6	**1a**	CH_2Cl_2	100/1/10	RT	52
7	**1a**	Toluene	500/1/10	RT	100
8	**1a**	Toluene	500/1/5	RT	100
9	**1a**	Toluene	1000/1/5	RT	77
10	**1a**	Toluene	1000/1/10	RT	61
11	**1a**	Toluene	1000/1/20	RT	49
12	**1a**	Toluene	1000/1/50	RT	34
13	**1a**	Toluene	500/1/10	40	82
14	**1a**	Toluene	1000/1/10	40	28
15	**1a**	*i*PrOH	500/1/10	60	19
16[b]	**1a**	Toluene	500/1/10	RT	100
17	**2a**	Toluene	500/1/10	RT	17
18	**2a**	Toluene	500/1/0	RT	0
19	**3a**	Toluene	500/1/0	RT	0

[a] Reactions performed under 20 bar H_2 with solvent and temperature specified with KO*t*Bu as a base, conversion was determined by ^{1}H NMR. [b] Mercury test.

no conversion (entry 19). We next examined the substrate scope for ketone hydrogenations using **1a** (Scheme 2). Notably, this compound displayed a broad substrate scope, reducing a variety of alkyl/aryl, dialkyl and diaryl ketones with conversion values exceeding 95 %. Worth to note, these results have been obtained with a lower catalyst loading and milder reaction conditions than those reported for other Mn(Br)(L–L)$(CO)_3$ precursors of non-bifunctional catalysts in these reactions (1–3 mol %, 30–50 °C, 50 bar H_2).[6a,11]

Due to the limited applications of non-bifunctional catalysts in the hydrogenation of aldehydes,[26] we also investigated the performance of compounds **1** in these reactions (Scheme 3). Hydrogenation of benzaldehyde under mild conditions (20 bar H_2, RT, toluene) using **1a** showed full conversion after 24 h. Product analysis indicated the preferential formation of benzyl alcohol, along with benzyl benzoate, resulting from a Tishchenko-type condensation,[27] with an alcohol/ester ratio (A/E) of 4.1 (entry 1, Table 2). Using **1b** led to a slightly lower conversion but a significant increase in the A/E ratio (entry 2). Increasing the temperature to 40 °C resulted in slightly higher selectivity (entry 3). We reasoned that the formation of the ester could be disfavoured by lowering the substrate concentration. Thus, the A/E ratio improved up to 23.0 (entry 4). The superior performance of **1b** was further confirmed by repeating the reaction with **1a** under the same conditions (entry 5). A blank reaction under these conditions showed nearly full conversion, but the ester as the main product (entry 6). Comparison of reactions of entries 4 and 6 clearly illustrates the significant impact of the catalyst on product selectivity. To further explore the utility of this catalytic system, we examined the hydrogenation of various aldehydes. Hydrogenation of several aryl aldehydes showed full conversion within 24 h and a good selectivity

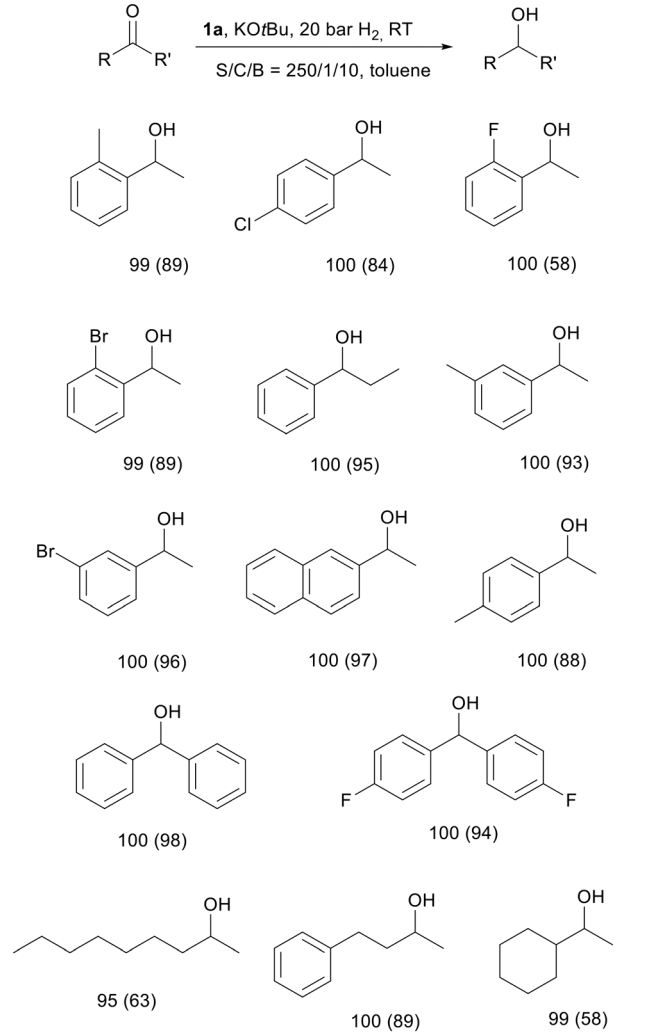

Scheme 2 Conversion (isolated yield in parentheses) values obtained in ketone hydrogenation reactions with **1a**.

towards the desired alcohol, with A/E ratios up to 50.0. A couple of α,β-unsaturated aldehydes were also tested. In

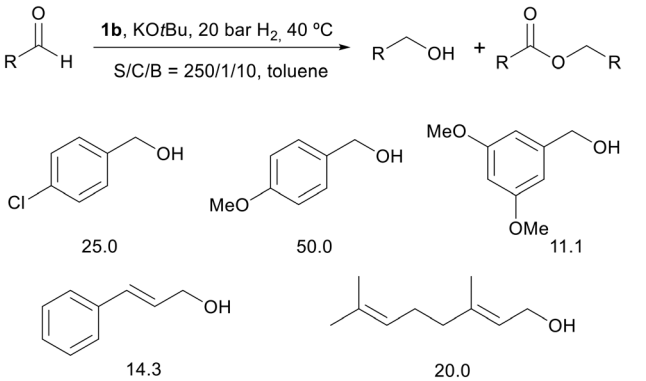

Scheme 3 Hydrogenation of aldehydes using complex **1b**. All reactions proceeded with full conversion. For aryl aldehydes the numerical values correspond to the alcohol/ester ratio. In the case of cinnamaldehyde and geranial, the values indicate the ratio between the allyl alcohol and the fully hydrogenated product.

Table 2 Hydrogenation of benzaldehyde with catalyst precursors **1a** and **1b**[a]

Entry	Complex	S/C/B	[S][b]	Temp. (°C)	Conv. (%)	Select (A/E)[c]
1	**1a**	500/1/10	1.1	RT	100	4.1
2	**1b**	500/1/10	1.2	RT	96	9.3
3	**1b**	500/1/10	1.2	40	100	11.5
4	**1b**	250/1/10	0.3	40	100	23.0
5	**1a**	250/1/10	0.3	40	100	6.8
6		250/0/10	0.3	40	98	0.1

[a] Reactions performed in toluene under 20 bar H_2, temperature specified with KO*t*Bu as a base. Conversion and selectivity were determined by ^{1}H NMR. [b] Substrate molar concentration. [c] Alcohol/ester ratio.

these cases, the preferential formation of the corresponding allyl alcohols was observed, with good selectivity.

Mechanistic spectroscopic results

An interesting aspect of catalytic hydrogenation using non-bifunctional [Mn(X)(L–L)(CO)$_3$] (X = Br, OTf, alkyl) complexes concerns their activation to generate the unsaturated hydride [Mn(H)(L–L)(CO)$_2$], which is responsible for catalysis. For complex **B**, it has been clearly shown that activation proceeds *via* migratory insertion followed by hydrogenolysis, leading to butyraldehyde and [Mn(H)(dippe)(CO)$_2$].[6d] Alternatively, it has been proposed that CO dissociation in [Mn(O^{s}Bu)(dippe)(CO)$_3$], followed by hydrogen coordination and alkoxide protonation can also lead to the active species.[7] In addition, the hydride [Mn(H)(H$_2$)(L–L)(CO)$_2$] has been proposed as the key species in reactions involving complex **D**, although the route leading to it is not fully understood.[10]

In light of the above, we investigated the activation of compounds **1** under hydrogenation conditions (Scheme 4). We observed that compound **1a** reacts with KO*t*Bu (3 equivalents) under 0.5 bar H_2 at room temperature in toluene-d_8. However, this reaction proceeds very slowly due to the low solubility of the base. The addition of 20 μL of THF to the NMR sample increased the reaction rate, showing *ca.* 30 % conversion after 1 h at room temperature. Alternatively, a faster reaction was observed is the base is dispersed by sonication (15 min; Fig. 6a and b; see SI for additional experiments). The reaction between **1a** and KO*t*Bu also took place in the absence of hydrogen, but resulted in a complex mixture, while no reaction between **1a** and H_2 was observed without base. Under H_2, the reaction with base is apparent from a colour change in the solution from yellow-orange to pale-yellow. In the hydride region of the ^{1}H NMR spectrum, a very broad hump composed by two overlapping broad signals at −8.6 and −9.4 ppm, and a doublet of doublets for **3a** in a 6 : 1 ratio, were detected (Fig. 7a). Lowering the temperature to −80 °C did not reach the slow exchange regime, although at −40 °C it was observed that the broad signal split into three still broad resonances centred at −7.6, −8.2, and −10.3 ppm in an approximate 1 : 3 : 2 ratio. In the ^{31}P{^{1}H} NMR spectrum at 25 °C (toluene-d_8), a broad signal appears in the phosphite region (201.8 ppm), along with two broad signals in the phosphine region (70.2 and 66.9 ppm), and doublets corresponding to **3a**, with unreacted **1a** present in a 6 : 1 : 3 ratio, respectively (Fig. 7b). At −40 °C, the phosphine region of the ^{31}P{^{1}H} NMR experiment also showed a splitting into three broad signals. These observations indicate the formation of a mixture of fluxional hydrides (**Hf**) upon the reaction of **1a** with KO*t*Bu under H_2. Exposure of this mixture

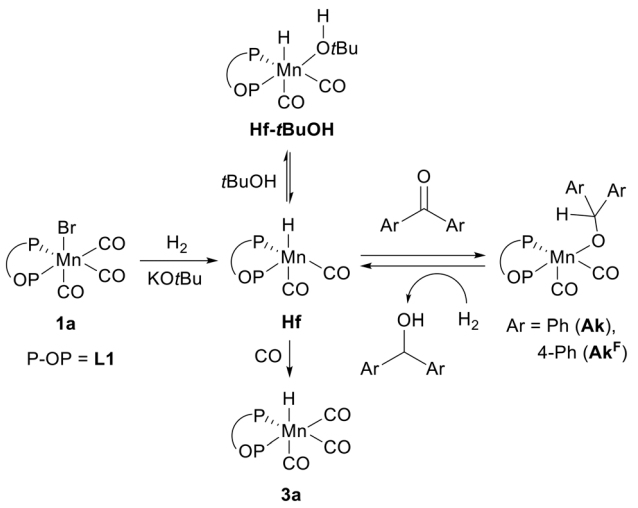

Scheme 4 Generation and reactions of key unsaturated Mn(H)(**L1**)(CO)$_2$ (**Hf**).

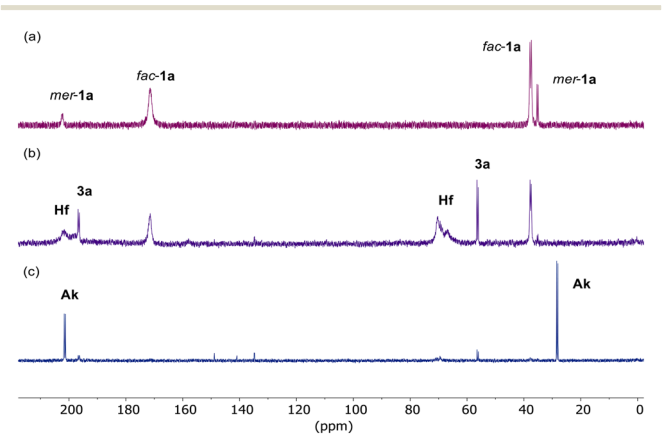

Fig. 6 ^{31}P{^{1}H} NMR (202 MHz, toluene-d_8): spectra of **1a** (a), activated **1a** by reaction with H_2 and KO*t*Bu after 15 min sonication (b), reaction of the latter with benzophenone (5 equiv., c).

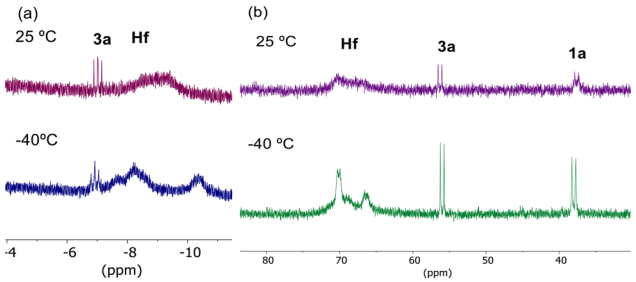

Fig. 7 ^{1}H (400 MHz, a) and $^{31}P\{^{1}H\}$ NMR (162 MHz, b) spectra of activated **1a** in toluene-d_8.

to a CO atmosphere leads to conversion into **3a**. After 15 min, the ratio of **Hf** to **3a** is 2 : 1, which evolves to 0.3 : 1 after 2 h. Alternatively, broad resonances centred at −9.1 and 1.0 ppm are observed in the ^{2}H NMR, in an approximate 1 : 1 ratio. The latter signal can be assigned to *t*BuOD, likely involved in a coordination/decoordination process. These experiments suggest that **Hf** corresponds to a mixture of isomers based on the Mn(H)(**L1**)$(CO)_2$ fragment which can be stabilized by solvent coordination. As well, computational studies show that these species can also be stabilized by an agostic interaction involving a *t*Bu group (see below).

Furthermore, **Hf** reacts with benzophenone (3–5 equiv.), turning the solution deep red. This reaction is evinced by the disappearance of the hydride signal in the ^{1}H NMR and the appearance of a very broad resonance at 5.65 ppm (5.44 ppm in the ^{2}H NMR for the deuteration experiment). In the $^{31}P\{^{1}H\}$ NMR, a set of narrow doublets centred at 201.4 and 28.3 ppm with $^{2}J_{PP}$ coupling constant of 87 Hz is observed (Fig. 6c). Upon reintroducing H_2 (0.5 bar), the solution fades to pale orange, the fluxional hydride signals reappeared in the ^{1}H NMR, and catalytic hydrogenation proceeded, yielding Ph_2CHOH. The aforementioned doublets in the $^{31}P\{^{1}H\}$ NMR remain visible until the latter stages of the reaction. Similarly, reaction of **Hf** with 4,4′-difluorobenzophenone yields two doublets in the $^{31}P\{^{1}H\}$ NMR at 201.3 and 28.5 ppm ($^{2}J_{PP}$ = 88 Hz), a broad signal in the ^{1}H NMR at 5.38 ppm, and two broad signals in the $^{19}F\{^{1}H\}$ NMR at −115.4 and −117.0 ppm (Fig. 8a and b). At low temperature, no appreciable changes were observed in the former signal while the latter splits into two singlets which appeared narrow at −40 °C at −116.5 and −117.0 ppm, corresponding to two non-equivalent ^{19}F nuclei (Fig. 8e), which parallel data reported by Baratta and coworkers for an Os–OCH(4-F-Ph)$_2$ alkoxide.[28] In turn, the signal at *ca.* −115 ppm should correspond to (4-F-Ph)$_2$CHOH generated from the residual H_2 present in solution. This signal appears broadened with respect to that of the free alcohol attributable to an exchange between free and coordinated alcohol. The signal at −117.0 ppm disappeared upon substrate consumption by reaction with H_2, raising the signal of the alcohol. Monitoring of the hydrogenation replenishing the H_2 atmosphere showed a clean hydrogenation (Fig. 8c and d). These results agree with the formation of alkoxides Mn(OCHAr$_2$)(**L1**)$(CO)_2$ (Ar = Ph (**Ak**), 4-F-Ph (**Ak^F**)) *via* reaction of **Hf** with the diarylketone, and

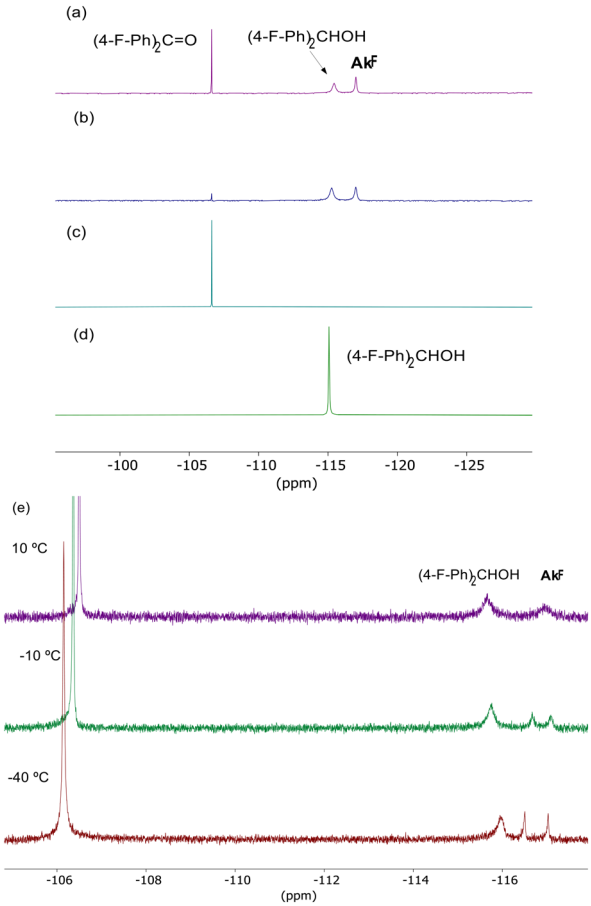

Fig. 8 $^{19}F\{^{1}H\}$ NMR (282 MHz, toluene-d_8) spectra of reaction between activated **1a** and 4,4′-difluorobenzophenone (1 equiv.) after 15 min (a); after 45 min (b). Reaction with 4,4′-difluorobenzophe-none (5 equiv.): immediately after ketone addition (c); after 6 h reaction under 0.5 bar H_2 (d). $^{19}F\{^{1}H\}$ NMR (376 MHz, toluene-d_8) VT spectra (e) of reaction between activated **1a** and 4,4′-difluorobenzophenone (5 equiv.).

subsequent hydrogenation to generate the corresponding diarylcarbinols. Attempts to isolate alkoxide intermediates were unsuccessful due to sample degradation during work-up.

Computational study

Catalyst activation. To support the experimental observations, we carried out DFT studies of the key steps involved in the activation of complexes **1**. As a reasonable starting point, we considered the formation of Mn(O*t*Bu)(**L1**)$(CO)_3$ (**4**) upon reaction of **1a** with KO*t*Bu.[29,30] According to literature precedents proposing either CO dissociation[7,23b] or alkoxide migration[31] in related alkoxide–diphosphine derivatives, we examined in detail both activation routes in alkoxide **4**. We studied the *fac1*, *fac2* and *mer1* isomers of **4**.[32] Among these, the *fac2* isomer was found to be the most stable, with *fac1* and *mer1* lying 2.9 and 6.5 kcal mol^{-1} higher in free energy, respectively.

In the CO dissociation route (Fig. 9), release of the CO ligand *trans* to the phosphite in *fac1*-**4** leading to a pentacoordinated

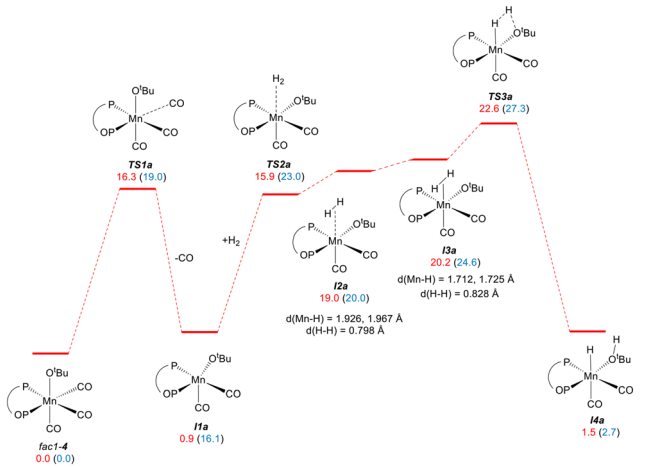

Fig. 9 General scheme for the activation of *fac1*-**4** by CO dissociation. Numerical values correspond to relative free (red) and electronic energies (blue, in parentheses) in kcal mol^{-1} relative to *fac1*-**4**.

alkoxide intermediate **I1a** is almost thermoneutral (ΔG = 0.9 kcal mol^{-1}) and proceeds with a moderate free energy barrier of 16.3 kcal mol^{-1} (**TS1a**). Hydrogen coordination to **Ia1** can take place either *trans* to CO or to the phosphite ligand. The former pathway, which locates the alkoxide *trans* to the phosphite fragment is energetically preferred and leads to a dihydrogen complex **I2a** which lays 19.0 kcal mol^{-1} above *fac1*-**4**. This complex features a rather unactivated H_2 ligand (d(Mn–H) = 1.926, 1.967 Å; d(H–H) = 0.798 Å). The subsequent alkoxide protonation step (**TS3a**) represents the highest overall barrier in this pathway ($\Delta G^{\ddagger}$ = 22.6 kcal mol^{-1}), yielding a hydride–*t*BuOH complex **I4a** (ΔG = 1.5 kcal mol^{-1}). IRC analysis of **TS3a** leads back to a dihydrogen complex **I3a** (ΔG = 20.2 kcal mol^{-1}) nearly isostructural to **I2a** but with a more activated H_2 ligand, as shown by Mn–H and H–H distances (d(Mn–H) = 1.712, 1.725 Å; d(H–H) = 0.828 Å). The small energy difference between **I2a** and **I3a** (*ca.* 1.2 kcal mol^{-1}) suggests facile interconversion between these species. Finally, hydride–alcohol complex **I4a** is expected to exchange readily the *t*BuOH ligand for a ketone. In the case of benzophenone, the equilibrium favours the k^1-*O* ketone adduct by 1.1 kcal mol^{-1}. The activation profile *via* CO dissociation parallels that reported by Beller and co-workers for *tert*-butoxide generated from **C** (R = H, R′ = Me), although the barriers found for *fac1*-**4** are around 5 kcal mol^{-1} lower.[10]

For the *fac2*-**4** isomer, CO dissociation also proceeds with a moderate barrier (**TS1b**, $\Delta G^{\ddagger}$ = 15.7 kcal mol^{-1}) in an endergonic step (5.4 kcal mol^{-1}), while for the least stable alkoxide *mer1*-**4**, the CO dissociation barrier is even lower (**TS1c**, $\Delta G^{\ddagger}$ = 8.0 kcal mol^{-1}) and the process slightly exergonic (−0.9 kcal mol^{-1}). Worth to note, the release of CO is accompanied by a significant shortening of the Mn–O bond (*e.g.* 2.206 Å in *fac1*-**4** *vs.* 1.839 in **I1a**). In contrast, significantly high barriers (ΔE > 30 kcal mol^{-1}) have been computed for the dissociation of CO in either *fac1* or *mer1* isomers of **1a** and **3a**. As in the profile depicted for *fac1*-**4**, alkoxide protonation remains the rate-limiting step in the cases of *fac2*-**4** and *mer1*-**4**, with corresponding **TS3b** and **TS3c** lying 2.6 and 2.3 kcal mol^{-1} in free energy above **TS3a**.

On the other hand, a lower-energy pathway was identified for the activation of **4** involving nucleophilic attack of the coordinated O*t*Bu on a CO ligand (Fig. 10).[33,34] In *fac1*-**4**, this attack to the CO ligand *trans* to phosphite (**TS1a′**) proceeds with a low barrier ($\Delta G^{\ddagger}$ = 9.1 kcal mol^{-1}), leading to a Mn–C bound carboxylate intermediate **I1a′** (ΔG = 4.6 kcal mol^{-1}). Hydrogen coordination yields a dihydrogen complex **I2a′** (ΔG = 5.4 kcal mol^{-1}), which undergoes protonation at the carboxylate carbon to form an H-bound formate complex **I3a′** (ΔG = 10.5 kcal mol^{-1}). This intermediate undergoes fast isomerisation to the O-bound formate **I4a′** (ΔG = −0.8 kcal mol^{-1}). The highest overall barriers in this pathway are associated with hydrogen coordination **TS2a′** and protonation **TS3a′** (both 13.0 kcal mol^{-1}), which compete favourably with those in the CO dissociation route. The alternative O*t*Bu migration pathway from the most stable alkoxide isomer *fac2*-**4** is less favourable, with a TS for carboxylate protonation (**TS3b′**) 4.7 kcal mol^{-1} higher in free energy than **TS3a′**. Finally, dissociation of *tert*-butyl formate from **I4a′** by *t*BuOH or benzophenone is thermodynamically favourable (ΔG = −2.9 and −4.1 kcal mol^{-1}, respectively). However, no *tert*-butyl formate was detected experimentally. We have observed that under reaction conditions used for catalyst activation, this ester reacts with KO*t*Bu to produce *t*BuOH and CO (see SI for further details),[35] the latter potentially responsible for the formation of Mn(H)(**L1**)$(CO)_3$ observed in experiments described above.

Benzophenone hydrogenation. We next examined the mechanism of ketone hydrogenation catalysed by the present system. To reduce the number of diastereomeric intermediates, we focused on the hydrogenation of benzophenone rather than acetophenone, as both substrates are readily hydrogenated by **1a**. As a reference, we followed the key features of the *inner-sphere* mechanism previously reported for acetophenone hydrogenation catalysed by Mn(H)(dippe)$(CO)_2$.[6d]

Initially, we considered isomers of the unsaturated hydride Mn(H)(**L1**)$(CO)_2$ (**5**, Fig. 11). Based on the activation mechanisms considered, formate dissociation in **I4a′** (or *t*BuOH release in **I4a**)

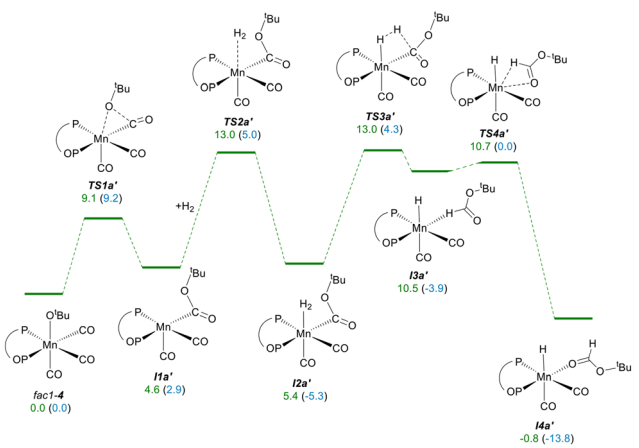

Fig. 10 General scheme for the activation of *fac1*-**4a** by O*t*Bu migration. Numerical values correspond to relative free (green) and electronic energies (blue, in parentheses) in kcal mol^{-1} relative to *fac1*-**4**.

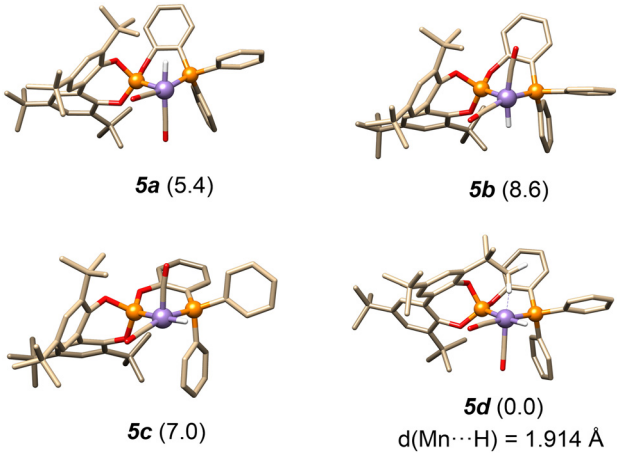

Fig. 11 Optimized geometries for Mn(H)(**L1**)$(CO)_2$ isomers (**5a**–**5d**). Numerical values correspond to relative free energies in kcal mol^{-1} relative to **5d**. Hydrogens have been omitted for clarity except those of the methyl involved in an agostic interaction in **5d**.

leads to the pentacoordinated hydride **5a**. Given the expected facile phosphite atropisomerisation, diastereotopic isomer **5b** was also considered.[36] A plausible isomerisation route involves hydride migration to the equatorial plane. This process is indeed feasible, with relatively low free energy barriers for the conversion of **5a** to **5d** (**TSad**: 9.8 kcal mol^{-1}) and **5b** to **5c** (**TSbc**: 11.7 kcal mol^{-1}). These results suggest a facile exchange between these unsaturated hydrides, consistent with spectroscopic observations. Among the isomers, **5d** is the more stable one as the result of an agostic interaction generated by a C–H of a *tert*-butyl substituent. Hydrides **5** adopt a distorted square planar geometry, with an available coordination site *trans* to either phosphite or a carbonyl ligand. Therefore, these species should readily coordinate an alcohol or carbonyl substrate to form the corresponding octahedral complexes. The hydrogenation pathway was examined for hydrides **5a**–**5d**, leading to four routes **a** to **d** (Fig. 12, Table 3). The reaction begins with formation of a hydride–ketone precomplex **I5**, which evolves *via* **TS5** to a k^1-*O*–benzophenone complex **I6**. This complex may isomerise through **TS6** to a k^2-*O*,*C* complex **I7**, which undergoes hydride insertion (**TS7**) to yield an agostic alkoxide **I8** (path **b**). Alternatively, hydride insertion can occur directly from **I6** (paths **a**, **c** and **d**). Release of the agostic interaction *via* **TS8** affords a pentacoordinated alkoxide **I9**, which is considerably more stable (ΔG = −2.5 to −15.2 kcal mol^{-1}) than the preceding agostic species. **I9** is suitable for hydrogen coordination (**TS9**), forming a dihydrogen–alkoxide complex **I10**. Finally, alkoxide protonation *via* **TS10** yields the hydride–alcohol complex **I11**. A notable feature of the mechanism is the remarkable stability of alkoxides **I9**, being **I9c** the most stable, $\Delta G°$ = −21.3 kcal mol^{-1} relative to the starting materials. According to the energy span model[37] analysis of these profiles, the turnover-determining intermediate (TDI) and turnover-determining transition states (TDTS) are **I9** and **TS10**, respectively, across all four cycles. The more favourable TS for alkoxide protonation corresponds to path **c** (**TS10c**), which also contains the most stable alkoxide **I9c**. Moreover, considering the small structural differences found among the **I9** alcoxides and their expected highly dynamic nature, it is reasonable to expect

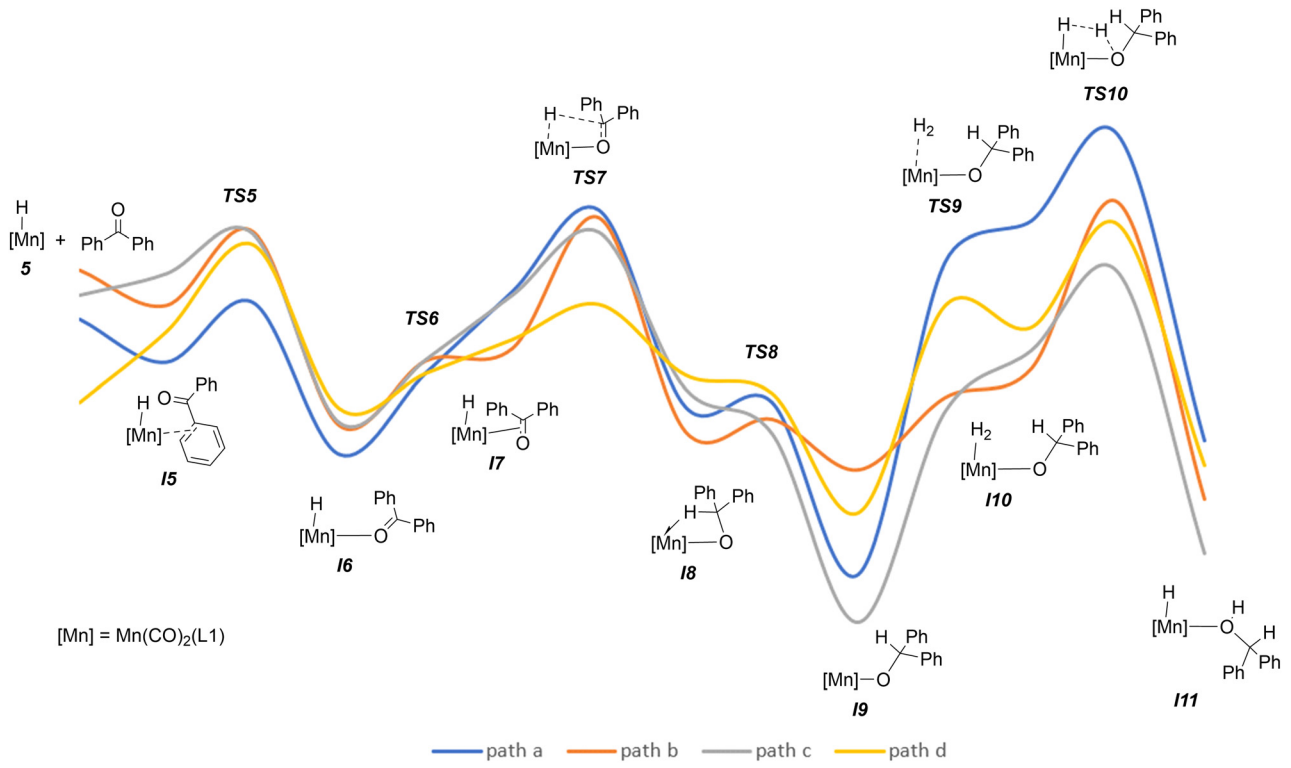

Fig. 12 Free energy profiles for benzophenone hydrogenation catalysed by Mn(H)(**L1**)$(CO)_2$.

Table 3 Calculated Energies for benzophenone hydrogenation catalysed by $Mn(CO)_2(H)$(**L1**) by paths **a** to **d**[a]

Species	ΔG (ΔE) (**a**)	ΔG (ΔE) (**b**)	ΔG (ΔE) (**c**)	ΔG (ΔE) (**d**)
5 + $Ph_2C{=}O$	−1.6 (−1.3)	1.6 (1.9)	0.0 (0.0)	−7.0 (−9.9)
I5	−4.4 (−22.8)	−0.6 (−20.5)	1.4 (−17.3)	-2.4 (−21.3)
TS5	−0.4 (−18.0)	4.1 (−14.2)	4.0 (−14.1)	3.4 (−13.5)
I6	−10.4 (−30.2)	−8.5 (−29.0)	−8.3 (−28.2)	−7.4 (−26.9)
TS6		−4.2 (−23.0)		
I7		−3.5 (−22.8)		
TS7	5.5 (−18.0)	5.0 (−13.7)	4.1 (−19.4)	−0.6 (−20.5)
I8	−7.3 (−30.1)	−8.9 (−29.5)	−6.1 (−26.4)	−5.2 (−28.8)
TS8	−7.0 (−27.4)	−8.1 (−29.5)	−8.9 (−29.5)	−6.4 (−26.3)
I9	−18.2 (−38.4)	−11.4 (−32.5)	−21.3 (−41.6)	−14.2 (−34.3)
TS9	2.1 (−27.2)	−6.7 (−35.5)	−7.6 (−36.7)	−0.7 (−29.8)
I10	4.8 (−30.9)	−3.2 (−37.6)	−3.6 (−39.5)	0.9 (−34.6)
TS10	10.4 (−20.1)	6.0 (−32.1)	1.5 (−29.9)	4.2 (−26.8)
I11	−9.4 (−43.8)	−13.3 (−48.2)	−16.8 (−51.8)	−11.5 (−45.4)

[a] Values in kcal mol^{-1} from **5c** + benzophenone.

that they can easily interconvert. Upon these considerations, it can be assumed that the dominant pathway in the catalysis will correspond to the formation of **I9c** and subsequent steps *via* path **c**. Accordingly, this alkoxide would be the resting state of the catalytic cycle, in agreement with the persistent observation of **Ak**/**Ak**$^{\mathbf{F}}$ species upon NMR monitoring of the catalytic hydrogenation.

Comparison with the dippe-based catalyst and alkoxide trap. Given the promising catalyst activity exhibited by **1a**, we compared its hydrogenation cycle with that of reference dippe-based catalyst. Using the same computational methodology, we calculated the hydrogenation profile of benzophenone catalysed by $Mn(H)(dippe)(CO)_2$ (see SI for details). The barrier for hydride migratory insertion is indeed found to be lower for dippe (1.1 kcal mol^{-1}) than for **L1** catalyst (4.1 kcal mol^{-1}). Moreover, the TS for the alkoxide protonation step is somewhat lower in free energy in the case of dippe (−0.6 *vs.* 1.5 kcal mol^{-1}), as well as the relevant pentacoordinated alkoxide (−21.7 *vs.* −21.3 kcal mol^{-1}). Overall, the energetic span[38] for the cycle of the dippe catalyst amounts 21.1 kcal mol^{-1}, only 1.7 kcal mol^{-1} lower than for **L1** catalyst (22.8 kcal mol^{-1}). From this small difference, within the accuracy of the DFT method,[39] it seems reasonable not to expect a remarkable difference in catalyst activity between both catalysts.[40]

Due to the strong metal–oxygen bonds, alkoxides can exhibit high stability, which may pose a severe drawback for catalysis. This has been related to donation from the lone pair on the alkoxide oxygen to a suitable unoccupied metal d orbital, resulting in a strong M–OR multiple bond. This effect is particularly critical in hydrogen borrowing reactions and the term *alkoxide trap* has been coined to describe it.[41] To explore this effect in our system, we examined the metal–alkoxide interaction in **I9c** in more detail. This intermediate adopts a distorted trigonal bipyramidal geometry (Fig. 13), with the phosphite, alkoxide and one CO ligand occupying the equatorial plane (P(phosphite)–Mn–O and $(CO)_{eq}$–Mn–O angles of 129.4° and 135.1°, respectively), while the apical positions are occupied by the other CO and the phosphine ligands (P(phosphine)–Mn–$(CO)_{ax}$ angle of 173.4°). Moreover, the Mn–O distance is significantly shorter than in the preceding agostic intermediate **I8c** (1.8436 Å *vs.* 1.9717 Å). A natural bonding orbital (NBO)[42] analysis revealed a Wiberg bond order of 0.51 for **I9c**, notably higher than the 0.36 found for **I8c**. In addition, second-order perturbation theory analysis indicated considerable donor–acceptor interactions between the alkoxide oxygen lone pairs of **I9c** and antibonding orbitals on Mn–C (carbonyl) and Mn–P (phosphite) (Fig. 14), with stabilisation energies (ΔE^2) of 25.6, 33.5 kcal mol^{-1} for the Mn–C and 48.3 kcal mol^{-1} for the Mn–P.[43] These findings agree with a particularly strong Mn–alkoxide interaction in **I9c**.

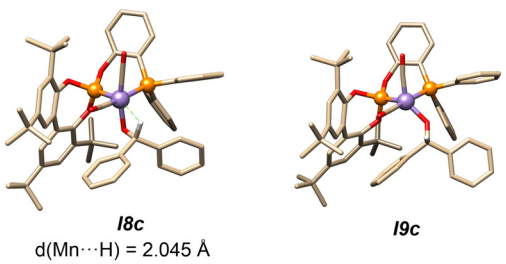

Fig. 13 Optimised geometries for alkoxide complexes **I8c** and **I9c** (all hydrogens except the alkoxide β one have been omitted for clarity).

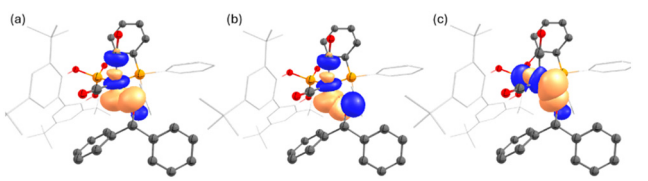

Fig. 14 Donor acceptor interactions between alkoxide oxygen lone pairs and Mn–C (carbonyl) (a and b) and Mn–P (phosphite) (c) antibonding orbitals in complex **I9c**.

Conclusions

In this contribution, we have described the synthesis and characterisation of Mn(I) complexes of the type Mn(Br)$(CO)_3$(P-OP) (**1**), bearing phosphine–phospite (P-OP) ligands. These complexes exist in solution as mixtures of the *fac* and *mer* isomers, with the *fac* one being predominant. IR spectroscopy data reflect the lower donor ability of P-OP ligands compared to bis(trialkylphosphines), which are commonly used in previously reported non-bifunctional Mn catalysts. Complexes **1** are effective in the hydrogenation of a broad range of aldehydes and ketones under mild conditions. A combined spectroscopic and computational study support a catalyst activation mechanism involving nucleophilic attack of the alkoxide on a coordinated CO ligand, as well as a non-bifunctional inner sphere hydrogenation pathway.

A key aspect of the catalytic cycle is the formation of a remarkably stable pentacoordinated alkoxide intermediate. This intermediate determines the energetic span of the cycle, rather that barriers associated with the more demanding hydride migration or alkoxide protonation steps. This feature, inherent to catalysts operating by an inner sphere mechanism, seems critical in catalyst activity. These results are of practical significance, as they suggest that a wide variety of potential Mn catalysts precursors can readily be prepared in a single step from Mn(Br)$(CO)_5$ and commercially available bidentate phosphorous ligands.[44] This modularity is particularly appealing for catalyst screening in asymmetric hydrogenation,[45] an area where most applications to date have relied on specifically designed PNP and PNN tridentate ligands for bifunctional catalysts.[46] Further studies on the scope and enantioselective applications of the Mn–POP catalysts reported herein are currently underway and will be disclosed in due course.

Conflicts of interest

There are no conflicts to declare.

Data availability

Supplementary Information: experimental details of the synthesis and characterization of Mn complexes and procedures for catalytic hydrogenation reactions. NMR spectra of mechanistic experiments, X-ray crystallographic data for **1a**, computational details and a coordinate file for structures calculated. See DOI: **https://doi.org/10.1039/D5CY00906E**.

CCDC 2468788 (**1a**) contains the supplementary crystallographic data for this paper.[47]

The data supporting this article have been included as part of the supplementary information (SI).

Conflicts of interest

There are no conflicts to declare.

Acknowledgements

We thank Ministerio de Ciencia, Innovación y Universidades from Spain (Grant PID2022-139782NB-I00/AEI/10.13039/501100011033/FEDER, UE) for financial support. The use of computational resources of the Centro Informático Científico de Andalucía (CICA, cluster Hércules) and the Galician Supercomputing Centre (CESGA) are also acknowledged.

Notes and references

1 (*a*) P. Chirik and R. Morris, *Acc. Chem. Res.*, 2015, **48**, 2495; (*b*) Y. Wang, L. Zhu, Z. Shao, G. Li, Y. Lan and Q. Liu, *J. Am. Chem. Soc.*, 2019, **141**, 17337–17349; (*c*) H. Zhao, A. K. Ravn, M. C. Haibach, K. M. Engle and C. C. C. J. Seechurn, *ACS Catal.*, 2024, **14**, 9708–9733; (*d*) M. Beller, *Chem. Rev.*, 2019, **119**, 2089.

2 (*a*) G. A. Filonenko, R. Van Putten, E. J. M. Hensen and E. A. Pidko, *Chem. Soc. Rev.*, 2018, **47**, 1459–1483; (*b*) G. A. Filonenko, R. Van Putten, E. J. M. Hensen and E. A. Pidko, *Chem. Soc. Rev.*, 2018, **47**, 1459–1483; (*c*) Y. Wang, M. Wang, Y. Li and Q. Liu, *Chem*, 2021, **7**, 1180–1223; (*d*) K. Das, S. Waiba, A. Jana and B. Maji, *Chem. Soc. Rev.*, 2022, **51**, 4386–4464; (*e*) K. Das, S. Waiba, A. Jana and B. Maji, *Chem. Soc. Rev.*, 2022, **51**, 4386–4464.

3 (*a*) S. Elangovan, C. Topf, S. Fischer, H. Jiao, A. Spannenberg, W. Baumann, R. Ludwig, K. Junge and M. Beller, *J. Am. Chem. Soc.*, 2016, **138**, 8809–8814; (*b*) F. Kallmeier, T. Irrgang, T. Dietel and R. Kempe, *Angew. Chem., Int. Ed.*, 2016, **55**, 11806–11809.

4 For studies on bifunctional catalysts containing ligands with NH fragments, see: (*a*) R. van Putten, E. A. Uslamin, M. Garbe, C. Liu, A. Gonzalez-de-Castro, M. Lutz, K. Junge, E. J. M. Hensen, M. Beller, L. Lefort and E. A. Pidko, *Angew. Chem., Int. Ed.*, 2017, **56**, 7531–7534; (*b*) S. Kar, A. Goeppert, J. Kothandaraman and G. K. S. Prakash, *ACS Catal.*, 2017, **7**, 6347–6351; (*c*) D. Wei, A. Bruneau-Voisine, T. Chauvin, V. Dorcet, T. Roisnel, D. A. Valyaev, N. Lugan and J. B. Sortais, *Adv. Synth. Catal.*, 2018, **360**, 676–681; (*d*) H. Li, D. Wei, A. Bruneau-Voisine, M. Ducamp, M. Henrion, T. Roisnel, V. Dorcet, C. Darcel, J. F. Carpentier, J. F. Soulé and J. B. Sortais, *Organometallics*, 2018, **37**, 1271–1279; (*e*) P. Ryabchuk, K. Stier, K. Junge, M. P. Checinski and M. Beller, *J. Am. Chem. Soc.*, 2019, **141**, 16923–16929; (*f*) Y. Wang, L. Zhu, Z. Shao, G. Li, Y. Lan and Q. Liu, *J. Am. Chem. Soc.*, 2019, **141**, 17337–17349; (*g*) M. B. Widegren and M. L. Clarke, *Catal. Sci. Technol.*, 2019, **9**, 6047–6058; (*h*) W. Yang, I. Y. Chernyshov, R. K. A. van Schendel, M. Weber, C. Müller, G. A. Filonenko and E. A. Pidko, *Nat. Commun.*, 2021, **12**, 1–8; (*i*) T. Vielhaber and C. Topf, *Appl. Catal., A*, 2021, **623**, 118280; (*j*) S. S. Gholap, A. Al Dakhil, P. Chakraborty, H. Li, I. Dutta, P. K. Das and K.-W. Huang, *Chem. Commun.*, 2021, **57**, 11815–11818; (*k*) D. Wei, R. Sang, P. Sponholz, H. Junge and M. Beller, *Nat. Energy*, 2022, **7**, 438–447; (*l*) V. Zubar, N. Lichtenberger, M. Schelwies, T. Oeser, A. S. K. Hashmi and T. Schaub, *ChemCatChem*, 2022, **14**,

e202101443; (*m*) Z. Wei, H. Li, Y. Wang and Q. Liu, *Angew. Chem., Int. Ed.*, 2023, **62**, e202301042.

5 For examples of catalysts based on a deprotonable CH ligand fragment see: (*a*) Y. Q. Zou, S. Chakraborty, A. Nerush, D. Oren, Y. Diskin-Posner, Y. Ben-David and D. Milstein, *ACS Catal.*, 2018, **8**, 8014–8019; (*b*) U. K. Das, A. Kumar, Y. Ben-David, M. A. Iron and D. Milstein, *J. Am. Chem. Soc.*, 2019, **141**, 12962–12966; (*c*) R. Buhaibeh, O. A. Filippov, A. Bruneau-Voisine, J. Willot, C. Duhayon, D. A. Valyaev, N. Lugan, Y. Canac and J. Sortais, *Angew. Chem., Int. Ed.*, 2019, **58**, 6727–6731; (*d*) S. M. W. Rahaman, D. K. Pandey, O. Rivada-Wheelaghan, A. Dubey, R. R. Fayzullin and J. R. Khusnutdinova, *ChemCatChem*, 2020, **12**, 5912–5918; (*e*) E. S. Gulyaeva, R. Buhaibeh, M. Boundor, K. Azouzi, J. Willot, S. Bastin, C. Duhayon, N. Lugan, O. A. Filippov, J. Sortais, D. A. Valyaev and Y. Canac, *Chem. – Eur. J.*, 2024, **30**, e202304201.

6 (*a*) S. Weber, B. Stöger and K. Kirchner, *Org. Lett.*, 2018, **20**, 7212–7215; (*b*) S. Weber, L. F. Veiros and K. Kirchner, *Adv. Synth. Catal.*, 2019, **361**, 5412–5420; (*c*) S. Kostera, S. Weber, M. Peruzzini, L. F. Veiros, K. Kirchner and L. Gonsalvi, *Organometallics*, 2021, **40**, 1213–1220; (*d*) S. Weber, J. Brünig, L. F. Veiros and K. Kirchner, *Organometallics*, 2021, **40**, 1388–1394; (*e*) R. A. Farrar-Tobar, S. Weber, Z. Csendes, A. Ammaturo, S. Fleissner, H. Hoffmann, L. F. Veiros and K. Kirchner, *ACS Catal.*, 2022, **12**, 2253–2260.

7 J. A. Garduño and J. J. García, *ACS Catal.*, 2019, **9**, 392–401.

8 M. Pinto, S. Friães, F. Franco, J. Lloret-Fillol and B. Royo, *ChemCatChem*, 2018, **10**, 2734–2740.

9 (*a*) K. Azouzi, L. Pedussaut, R. Pointis, A. Bonfiglio, R. Kumari Riddhi, C. Duhayon, S. Bastin and J.-B. Sortais, *Organometallics*, 2023, **42**, 1832–1838; (*b*) K. Azouzi, R. Pointis, R. Buhaibeh, P. H. Fernández, L. Pedussaut, M. Boundor, A. Bonfiglio, A. Bruneau-Voisine, D. Wei, T. Roisnel, C. Duhayon, M. Á. Casado, D. A. Valyaev, Y. Canac, S. Bastin, C. Raynaud and J.-B. Sortais, *J. Catal.*, 2024, **430**, 115334.

10 N. F. Both, A. Spannenberg, H. Jiao, K. Junge and M. Beller, *Angew. Chem., Int. Ed.*, 2023, **62**, e202307987.

11 M. Hruzd, S. L. Kleynemeyer, C. Michon, S. Bastin, E. Pollet, V. Ritleng and J. B. Sortais, *Chem. Commun.*, 2025, 2969–2972.

12 For reviews on this topic see: (*a*) P. W. N. M. van Leeuwen, P. C. J. Kamer, C. Claver, O. Pàmies and M. Diéguez, *Chem. Rev.*, 2010, **111**, 2077–2118; (*b*) J. F. Teichert and B. L. Feringa, *Angew. Chem., Int. Ed.*, 2010, **49**, 2486–2528; (*c*) D. S. Surry and S. L. Buchwald, *Angew. Chem., Int. Ed.*, 2008, **47**, 6338–6361; (*d*) A. L. Clevenger, R. M. Stolley, J. Aderibigbe and J. Louie, *Chem. Rev.*, 2020, **120**, 6124–6196.

13 See, for instance: (*a*) Z. L. Niemeyer, A. Milo, D. P. Hickey and M. S. Sigman, *Nat. Chem.*, 2016, **8**, 610–617; (*b*) J. Tian, G. Wang, Z. Qi and J. Ma, *ACS Omega*, 2020, **5**, 21385–21391; (*c*) C. Li, R. Dickson, N. Rockstroh, J. Rabeah, A. Spannenberg, M. Bühl and E. Mejía, *Catal. Sci. Technol.*, 2020, **10**, 7745–7756.

14 (*a*) S. Vargas, M. Rubio, A. Suárez, D. del Río, E. Álvarez and A. Pizzano, *Organometallics*, 2006, **25**, 961–973; (*b*) M. Á. Chávez, S. Vargas, A. Suárez, E. Álvarez and A. Pizzano, *Adv. Synth. Catal.*, 2011, **353**, 2775–2794; (*c*) M. Vaquero, S. Vargas, A. Suárez, S. E. García-Garrido, E. Álvarez, M. Mancera and A. Pizzano, *Organometallics*, 2012, **31**, 3551–3564; (*d*) M. Vaquero, A. Suárez, S. Vargas, G. Bottari, E. Álvarez and A. Pizzano, *Chem. – Eur. J.*, 2012, **18**, 15586–15591; (*e*) P. Kleman, P. J. González-Liste, S. E. García-Garrido, V. Cadierno and A. Pizzano, *ACS Catal.*, 2014, **4**, 4398–4408; (*f*) P. J. González-Liste, F. León, I. Arribas, M. Rubio, S. E. García-Garrido, V. Cadierno and A. Pizzano, *ACS Catal.*, 2016, **6**, 3056–3060.

15 (*a*) K. Nozaki, N. Sakai, T. Nanno, T. Higashijima, S. Mano, T. Horiuchi and H. Takaya, *J. Am. Chem. Soc.*, 1997, **119**, 4413–4423; (*b*) F. Doro, J. N. H. Reek and P. W. N. M. van Leeuwen, *Organometallics*, 2010, **29**, 4440–4447; (*c*) H. Fernández-Pérez, J. Benet-Buchholz and A. Vidal-Ferran, *Chem. – Eur. J.*, 2014, **20**, 15375–15384.

16 (*a*) M. Diéguez, S. Deerenberg, O. Pàmies, C. Claver, P. W. N. M. Van Leeuwen and P. Kamer, *Tetrahedron: Asymmetry*, 2000, **11**, 3161–3166; (*b*) T. Robert, J. Velder and H.-G. Schmalz, *Angew. Chem., Int. Ed.*, 2008, **47**, 7718–7721; (*c*) W. Lölsberg, S. Ye and H.-G. Schmalz, *Adv. Synth. Catal.*, 2010, **352**, 2023–2031.

17 Q. Du, J. M. Neudörfl and H. G. Schmalz, *Chem. – Eur. J.*, 2018, **24**, 2379–2383.

18 (*a*) T. Horiuchi, E. Shirakawa, K. Nozaki and H. Takaya, *Tetrahedron: Asymmetry*, 1997, **8**, 57–63; (*b*) A. Falk, A.-L. Göderz and H.-G. Schmalz, *Angew. Chem., Int. Ed.*, 2013, **52**, 1576–1580.

19 A. Pizzano, *Chem. Rec.*, 2016, **16**, 2595–2618.

20 (*a*) M. Rubio, S. Vargas, A. Suárez, E. Álvarez and A. Pizzano, *Chem. – Eur. J.*, 2007, **13**, 1821–1833; (*b*) F. León, A. Comas-Vives, E. Álvarez and A. Pizzano, *Catal. Sci. Technol.*, 2021, **11**, 2497–2511.

21 M. F. Brown, B. R. Cook and T. E. Sloan, *Inorg. Chem.*, 1975, **14**, 1273–1278.

22 A. Suarez, M. A. Mendez-Rojas and A. Pizzano, *Organometallics*, 2002, **21**, 4611–4621.

23 (*a*) S. J. A. Pope and G. Reid, *J. Chem. Soc., Dalton Trans.*, 1999, 1615–1621; (*b*) J. A. Garduño, M. Flores-Alamo and J. J. García, *ChemCatChem*, 2019, **11**, 5330–5338.

24 B. S. Ault, T. M. Becker, G. Q. Li and M. Orchin, *Spectrochim. Acta, Part A*, 2004, **60**, 2567–2572.

25 Calculations have been done using the ORCA program (version 5.0.3) using BP86 functional with def2-SVP basis set along with auxiliary bases def2/J, using CPCM model to include solvent effects (benzene for compounds **1** and **3** and toluene for catalytic studies) and dispersion correction (Grimme D3) in a first stage. Structures obtained were recalculated using B3PW91 functional and def2-TZVP basis set with def2/J auxiliary basis along with mentioned dispersion and solvent corrections. Molecular structures have been generated with Chimera software (see SI for further details).

26 To the best of our knowledge, precedents of these reactions are limited to hydrogenation of a couple of α,β-unsaturated aldehydes reported in ref. 6*d*.

27 S. Baldino, S. Facchetti, A. Zanotti-Gerosa, H. G. Nedden and W. Baratta, *ChemCatChem*, 2016, **8**, 2279–2288.

28 W. Baratta, M. Ballico, G. Chelucci, K. Siega and P. Rigo, *Angew. Chem., Int. Ed.*, 2008, **47**, 4362–4365.
29 (*a*) C. Liu, R. van Putten, P. O. Kulyaev, G. A. Filonenko and E. A. Pidko, *J. Catal.*, 2018, **363**, 136–143; (*b*) R. van Putten, G. A. Filonenko, A. G. de Castro, C. Liu, M. Weber, C. Müller, L. Lefort and E. Pidko, *Organometallics*, 2019, **38**, 3187–3196.
30 For examples on the formation of tert-butoxide-phosphine complexes upon reaction between halo precursors and KOtBu, see: (*a*) W. Baratta, M. Ballico, A. Del Zotto, E. Herdtweck, S. M. R. Peloso, K. Siega, M. Toniutti, E. Zangrando and P. Rigo, *Organometallics*, 2009, **28**, 4421–4430; (*b*) E. Z. Jahromi and J. Gailer, *Dalton Trans.*, 2010, **39**, 329–336; (*c*) M. C. MacInnis, R. McDonald, M. J. Ferguson, S. Tobisch and L. Turculet, *J. Am. Chem. Soc.*, 2011, **133**, 13622–13633; (*d*) A. Adhikary, J. A. Krause and H. Guan, *Organometallics*, 2015, **34**, 3603–3610.
31 S. Weber and K. Kirchner, *Acc. Chem. Res.*, 2022, **55**, 2562–2580.
32 For a study of the relative reactivity of fac/mer isomers in $Mn(H)(dppm)(CO)_3$ see: E. S. Osipova, E. S. Gulyaeva, N. V. Kireev, S. A. Kovalenko, C. Bijani, Y. Canac, D. A. Valyaev, O. A. Filippov, N. V. Belkova and E. S. Shubina, *Chem. Commun.*, 2022, 5017–5020.
33 For a study of nucleophilic additions of alkoxides to metal carbonyls see: R. van Putten, G. A. Filonenko, A. M. Krieger, M. Lutz and E. A. Pidko, *Organometallics*, 2021, **40**, 674–681.
34 Worth to note an analogous activation route from Mn(Br)(N, N′-dimethyl-1,2-cyclohexanediamine)$(CO)_3$ and KOiPr has been proposed: A. Hashemi, S. Bougueroua, M.-P. Gaigeot and E. A. Pidko, *J. Chem. Theory Comput.*, 2022, **18**, 7470–7482.
35 J. C. Powers, R. Seidner, T. G. Parsons and H. J. Berwin, *J. Org. Chem.*, 1966, **31**, 2623–2627.
36 Atropisomerization of **5a** would lead to a diastereomeric hydride with the same configuration at the metal and R_{ax} configuration at the biaryl. Instead of the latter, **5b** which is enantiomeric with atropisomerized **5a** has been considered to keep the S_{ax} biaryl configuration fixed along the study.
37 S. Kozuch and S. Shaik, *Acc. Chem. Res.*, 2011, **44**, 101–110.
38 Calculated with the AUTOF software: A. Uhe, S. Kozuch and S. Shaik, *J. Comput. Chem.*, 2011, **32**, 978–985.
39 P. A. Dub, N. J. Henson, R. L. Martin and J. C. Gordon, *J. Am. Chem. Soc.*, 2014, **136**, 3505–3521.
40 Our standard conditions use a lower catalyst loading and milder reaction conditions than those reported for A (ref. 6*a*), although from results reported for B (ref. 6*c*) it may be inferred a higher activity for $Mn(H)(dippe)(CO)_2$. Unfortunately, we have not found data at lower catalyst loading for the dippe system to directly compare it with that of **1a**.
41 (*a*) Z. Ye, Z. Yang, C. Yang, M. Huang, X. Xu and Z. Ke, *Org. Chem. Front.*, 2022, **9**, 4803–4817; (*b*) P. Su, Z. Chen, J. Ni, Z. Yang, Y. Li and Z. Ke, *ACS Catal.*, 2023, **13**, 12481–12493; (*c*) A. Vignesh, Z. Wang, Y. Liu and Z. Ke, *ChemCatChem*, 2024, **16**, e202400821.
42 E. D. Glendening, J. K. Badenhoop, A. E. Reed, J. E. Carpenter, J. A. Bohmann, C. M. Morales, P. Karafiloglou, C. R. Landis and F. Weinhold, *NBO 7.0.*, Theoretical Chemistry Institute, University of Wisconsin, Madison, 2018.
43 (*a*) S. D. Pike, F. M. Chadwick, N. H. Rees, M. P. Scott, A. S. Weller, T. Krämer and S. A. Macgregor, *J. Am. Chem. Soc.*, 2015, **137**, 820–833; (*b*) M. A. Sajjad, J. A. Harrison, A. J. Nielson and P. Schwerdtfeger, *Organometallics*, 2018, **37**, 3659–3669; (*c*) M. Navarro, A. Toledo, S. Mallet-Ladeira, E. D. Sosa Carrizo, K. Miqueu and D. Bourissou, *Chem. Sci.*, 2020, **11**, 2750–2758.
44 M. Renom-Carrasco and L. Lefort, *Chem. Soc. Rev.*, 2018, **47**, 5038–5060.
45 (*a*) M. R. Friedfeld, H. Zhong, R. T. Ruck, M. Shevlin and P. J. Chirik, *Science*, 2018, **360**, 888–893; (*b*) M. J. Lebowitz, C. S. MacNeil, L. N. Mendelsohn, M. Shevlin, M. V. Pecoraro, G. Hierlmeier and P. J. Chirik, *ACS Catal.*, 2024, **14**, 13260–13268.
46 (*a*) M. B. Widegren, G. J. Harkness, A. M. Z. Slawin, D. B. Cordes and M. L. Clarke, *Angew. Chem., Int. Ed.*, 2017, **56**, 5825–5828; (*b*) M. Garbe, K. Junge, S. Walker, Z. Wei, H. Jiao, A. Spannenberg, S. Bachmann, M. Scalone and M. Beller, *Angew. Chem., Int. Ed.*, 2017, **56**, 11237–11241; (*c*) L. Zhang, Y. Tang, Z. Han and K. Ding, *Angew. Chem., Int. Ed.*, 2019, **58**, 4973–4977; (*d*) F. Ling, H. Hou, J. Chen, S. Nian, X. Yi, Z. Wang, Di. Song and W. Zhong, *Org. Lett.*, 2019, **21**, 3937–3941; (*e*) L. Zhang, Z. Wang, Z. Han and K. Ding, *Angew. Chem., Int. Ed.*, 2020, **59**, 15565–15569; (*f*) L. Zeng, H. Yang, M. Zhao, J. Wen, J. H. R. Tucker and X. Zhang, *ACS Catal.*, 2020, **10**, 13794–13799; (*g*) C. Liu, M. Wang, S. Liu, Y. Wang, Y. Peng, Y. Lan and Q. Liu, *Angew. Chem., Int. Ed.*, 2021, **60**, 5108–5113; (*h*) C. S. G. Seo, B. T. H. Tsui, M. V. Gradiski, S. A. M. Smith and R. H. Morris, *Catal. Sci. Technol.*, 2021, **11**, 3153–3163.
47 CCDC 2468788: Experimental Crystal Structure Determination, 2025, DOI: **10.5517/ccdc.csd.cc2mdsmg**.